

A Cloudy Fit to the Atmosphere of WASP-107 b

Helong Huang (黄赫龙)^{1,*}, Michiel Min², Chris W. Ormel¹, Achène Dyrek³, and Nicolas Crouzet^{4,5}

¹ Department of Astronomy, Tsinghua University, Haidian DS 100084 Beijing, China

² SRON Netherlands Institute for Space Research, Niels Bohrweg 4, 2333CA Leiden, The Netherlands

³ Space Telescope Science Institute, Baltimore, Maryland, USA

⁴ Kapteyn Astronomical Institute, University of Groningen, P.O. Box 800, 9700 AV Groningen, The Netherlands

⁵ Leiden Observatory, Leiden University, P.O. Box 9513, 2300 RA Leiden, The Netherlands

Received September 15, 1996; accepted March 16, 1997

ABSTRACT

Context. WASP-107 b has been observed comprehensively by JWST in the near- and mid-IR bands, making it an ideal planet to probe the composition and internal dynamics. Recent analysis reveals a 8 – 10 μm silicate feature, but it still remains uncertain how silicate clouds form on this planet.

Aims. We aim at fitting the complete JWST spectrum of WASP-107 b, from 0.9 μm to 12 μm with a physically motivated cloud model and self-consistent temperature profile.

Methods. Two-stream radiative transfer is coupled to a cloud formation model until convergence between cloud and temperature profiles is reached. We search a model grid spanning metallicity, turbulent diffusivity, internal heat flux and nucleation parameters to find the best fit model.

Results. The silicate cloud feature at 10 μm and the near-IR molecular band strength can be simultaneously and naturally explained without assuming a parametrized temperature profile. A moderate vertical diffusivity of $K_{zz}=10^9 \text{ cm}^2\text{s}^{-1}$ is needed to bring the cloud particles to the upper atmosphere of WASP-107 b. This K_{zz} is favored by the joint fitting of the near-IR water feature and mid-IR silicate feature – both sensitive to clouds. From the strength of H₂O and CO₂ bands, our model suggests a metallicity 17 times solar.

Conclusions. Even in warm planets such as WASP-107 b, silicate clouds can form in the relatively cool upper atmosphere because turbulence uplifts vapor and cloud particles. Despite having considerably fewer degrees of freedom, the self-consistent modeling approach successfully fits WASP-107b's multi-wavelength data, instilling confidence in the derived physical parameters.

Key words. Planets and satellites: atmospheres – Planets and satellites: gaseous planets – Planets and satellites: individual: WASP-107 b

1. Introduction

WASP-107 b is a warm, super-Neptune-mass planet around a K6 star. It has a size of 0.95 R_{Jup} and is on a 5.7-day orbit (Ander-son et al. 2017). Follow-up RV measurement refined its mass to $30.5 \pm 1.7 M_{\oplus}$ (Piaulet et al. 2021). WASP-107 b's large radius makes it an ideal target to observe the transmission spectrum, because the large planet-to-star radius ratio magnifies the spectral features. The HST transmission spectrum of this planet shows water feature and cloud extinction in the near-IR (Kreidberg et al. 2018). Recently, JWST NIRCам and NIRSpec has found H₂O, CO₂, SO₂, CO, NH₃ and CH₄ on WASP-107 b with high confidence levels (Welbanks et al. 2024; Sing et al. 2024, W24 and S24 hereafter). Furthermore, both JWST and HST have found He absorption around the transit, indicating ongoing atmospheric escaping process on this planet (Spake et al. 2018; Krishnamurthy et al. 2025, K25 hereafter).

With the observations from JWST, clouds on WASP-107 b are found at all wavelengths from 2.4 μm to 12 μm . S24 showed that clouds are needed to lift the transit depth between 3.6 and 4.0 μm . Dyrek et al. (2024) found that the JWST/MIRI observation clearly favors the presence of silicate clouds, hinted by the 10 μm Si–O stretching feature. Their retrieval suggested the presence of submicron sized cloud particles at the $\sim 10^{-4}$ bar level. However, at those cool layers, it is believed that any sil-

icates would have rained out to deeper, hotter region. On the other hand, from the depletion of CH₄, it has been found that the atmosphere of WASP-107 b is characterized by strong turbulence (S24), which could potentially transport particles up into the visible atmosphere.

Most previous works fit the transmission spectrum of WASP-107 b with parameterized cloud properties. For example, S24 applied gray clouds and a power-law haze opacity to retrieve the 2.6 to 5.2 μm NIRSpec spectrum. Dyrek et al. (2024) used realistic optical properties of silicates, but parameterized the vertical distribution of clouds. Also, W24 used an additional opacity with skewed Gaussian shape along the wavelength dimension to mimic the mid-IR silicate opacity. Even though these cloud parameterizations provided successful fits to the spectra, the question how silicate clouds form in the atmosphere of WASP-107 b has not yet been addressed.

Therefore we aim to investigate whether the cloud features on WASP-107 b can be understood with a realistic cloud formation model. Instead of parameterizing cloud properties, we simulate the cloud formation on WASP-107 b with the physically-motivated cloud model ExoLyn (Huang et al. 2024). This allows us to identify which silicate species the cloud particles are composed of. In addition, the temperature is calculated with a two-stream radiative transfer model that accounts for both molecular and cloud opacities (Huang et al., in prep.). Our model results are compared with the transmission spectrum taken by

* Corresponding author: huanghl22@mails.tsinghua.edu.cn

Table 1. Parameters of the grid search. The highlighted ones indicate the best-fit.

Parameter	grid values					Unit
$\log Z/Z_{\odot}$	0.5	0.75	1	1.25	1.5	
K_{zz}	10^8	$10^{8.5}$	10^9	$10^{9.5}$	10^{10}	$\text{cm}^2 \text{s}^{-1}$
T_{int}	350	450	550	-	-	K
$\dot{\Sigma}_{\text{nuc}}$	10^{-21}	10^{-20}	10^{-19}	10^{-18}	10^{-17}	$\text{g cm}^{-2} \text{s}^{-1}$
P_{nuc}	10^{-4}	10^{-3}	10^{-2}	10^{-1}	-	bar

JWST/NIRISS (K25), NIRCcam (W24) and MIRI (Dyrek et al. 2024), covering visible to mid-IR wavelengths. Data at wavelengths $\lambda < 1 \mu\text{m}$ and $2\text{--}2.5 \mu\text{m}$ are excluded, as they may be affected by the transit light source effect (K25). The NIRCcam data, from $2.5 \mu\text{m}$ to $5 \mu\text{m}$, used in this study does not show evidence for starspot crossing event (W24). Beyond $\lambda > 2.5 \mu\text{m}$ the effect of starspots is decreasing with wavelength (Rackham et al. 2018). Therefore, the effect of transit light source on our findings is minor.

2. Results

We couple the cloud model ExoLyn with two-stream radiative transfer to get a self-consistent TP profile and cloud structure. Our model is summarized in the Appendix A and the details are described in Huang et al. (2024) and a companion paper. We construct a grid of parameters (Table 1), with varying metallicity Z , vertical turbulent diffusivity K_{zz} , effective temperature of the internal emission flux T_{int} , nuclei injection rate $\dot{\Sigma}_{\text{nuc}}$ and nucleation depth P_{nuc} to find the parameters that best match the observations, including the mid-IR silicate features and near-IR molecular band strength. For each parameter combination, we adjust the equilibrium gas composition to account for the vertical mixing and sulfur photochemistry, which are described in the Appendix A.2. The observational data combining JWST/NIRISS (K25), JWST/NIRCcam and JWST/MIRI presented in W24, covers a broad wavelength range between $0.85\text{--}12 \mu\text{m}$. The best fit model is found with $Z = 17 Z_{\odot}$, $K_{zz} = 10^9 \text{ cm}^2 \text{ s}^{-1}$, $T_{\text{int}} = 550 \text{ K}$, $P_{\text{nuc}} = 10^{-3} \text{ bar}$ and $\dot{\Sigma}_{\text{nuc}} = 10^{-20} \text{ g cm}^{-2} \text{ s}^{-1}$.

The converged TP profile and the cloud structure are shown in Figure 1. For the best-fit $K_{zz} = 10^9 \text{ cm}^2 \text{ s}^{-1}$ run, the upper cloud layer is dominated by SiO_2 , until 0.3 bar, where the dominant species changes to MgSiO_3 , Mg_2SiO_4 and Fe because the temperature is high enough for SiO_2 to evaporate. Due to gravitational settling, the cloud mixing ratio peaks at 0.2 bar. Clouds evaporate at a pressure of 0.6 bar where $T \approx 2200 \text{ K}$. At $2 \times 10^{-3} \text{ bar}$ and $5 \times 10^{-3} \text{ bar}$ the atmosphere becomes optically thick to the stellar IR and visible photons. Here, the cloud particles reach sizes of $\sim \mu\text{m}$. Increasing K_{zz} does not change the dominant cloud species (SiO_2), but does lead to more vertically extended clouds. This is because vapor gets replenished more efficiently in the cloud forming region and the cloud particles undergo stronger updraft motion. The photospheric temperature we obtain (730 K) agrees with the retrieved values in K25 ($\sim 700 \text{ K}$) and lies in between the radiative-convective-equilibrium models presented by W24 ($\sim 500 \text{ K}$) and S24 ($\sim 800 \text{ K}$).

Figure 2 shows the synthetic transmission spectrum compared to observations. We also plot the simulation results obtained by varying the vertical turbulent diffusivity K_{zz} with respect to the best-fit model to demonstrate how this parameter affects the silicate features in the spectrum. The black solid line shows the transmission spectrum corresponding to the best-fit $K_{zz} = 10^9 \text{ cm}^2 \text{ s}^{-1}$ run. Our model provides a good match to the strength of both the near-IR molecular bands and the mid-

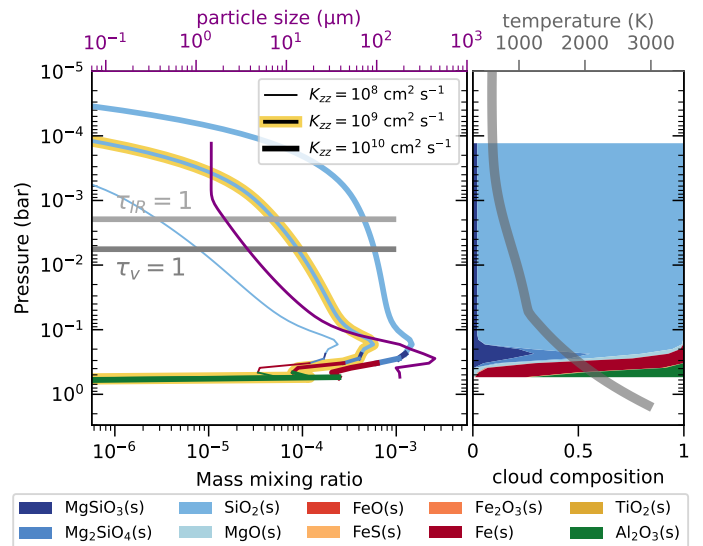


Fig. 1. Self-consistent temperature and cloud profiles, resulting from the joint cloud and radiative transfer model. Left: cloud profiles obtained for three K_{zz} values. The best fit model has $K_{zz} = 10^9 \text{ cm}^2 \text{ s}^{-1}$ (the line with golden highlight) and the corresponding particle size is shown by the purple line. The horizontal gray lines indicates the visible and IR photosphere. Right: cloud composition by mass fraction of the best-fit model. The gray line shows the atmosphere temperature profile of the best fit.

IR silicate feature. Compared to the clear spectrum, SiO_2 clouds give rise to enhanced absorption at 8 to $10 \mu\text{m}$. In the near-IR, scattering by μm -sized particles raises the transit depth at wavelengths below $2.5 \mu\text{m}$, suppressing the 1.2, 1.5, 1.9 and $2.8 \mu\text{m}$ H_2O features. Besides H_2O , other molecular features are also reproduced. The atmospheric metallicity affects the strength of the $4.4 \mu\text{m}$ CO_2 feature, and is constrained at $\approx 17 Z_{\odot}$. Our model also reproduces the SO_2 feature at $7.4 \mu\text{m}$ under the assumption of a 9×10^{-3} conversion ratio from H_2S to SO_2 . This conversion is applied to mimic the effects of photochemistry (not included in our model), which is believed to be the cause of the presence of SO_2 on hot Jupiters (Tsai et al. 2023, W24).

Varying the turbulent diffusivity parameter leads to vertical shifts in the transmission spectrum. When $K_{zz} = 10^{10} \text{ cm}^2 \text{ s}^{-1}$, clouds are more extended. In this case, cloud extinction $< 2 \mu\text{m}$ is too strong and the transit depth is overestimated compared to the observations. On the other hand, when $K_{zz} = 10^8 \text{ cm}^2 \text{ s}^{-1}$, clouds settle too deep, leading to a nearly invisible silicate feature and larger near-IR water line amplitudes. In conclusion, the cloud features at $1\text{--}4 \mu\text{m}$ and $8\text{--}10 \mu\text{m}$ can be reproduced only with a turbulent diffusivity $K_{zz} = 10^9 \text{ cm}^2 \text{ s}^{-1}$, consistent with the value inferred from the gas-phase disequilibrium chemistry model used in W24 and Changeat et al. (2025).

In Figure 3 we show how the K_{zz} , T_{int} and Z parameters change the spectroscopic features that are affected by clouds. To analyze the clouds' ability to mute molecular lines, we measure the strength of the $1.4 \mu\text{m}$ H_2O band. We take the water line strength metric in Stevenson (2016):

$$f_{\text{water}} = (\eta^{\text{water}} - \eta^{\text{cont}}) / \eta^{\text{cont}}, \quad (1)$$

where η^{water} is the transit depth at the peak of the H_2O band (i.e., $1.36\text{--}1.44 \mu\text{m}$) and η^{cont} is that at the continuum wavelengths (i.e., $1.22\text{--}1.3 \mu\text{m}$). In addition to f_{water} , we quantify the strength of the $10 \mu\text{m}$ silicate feature through a silicate metric f_{silicate} , obtained by decomposing the transmission spectrum from $8.4\text{--}10.1 \mu\text{m}$ into Legendre polynomials up to second order: $\eta(\lambda) =$

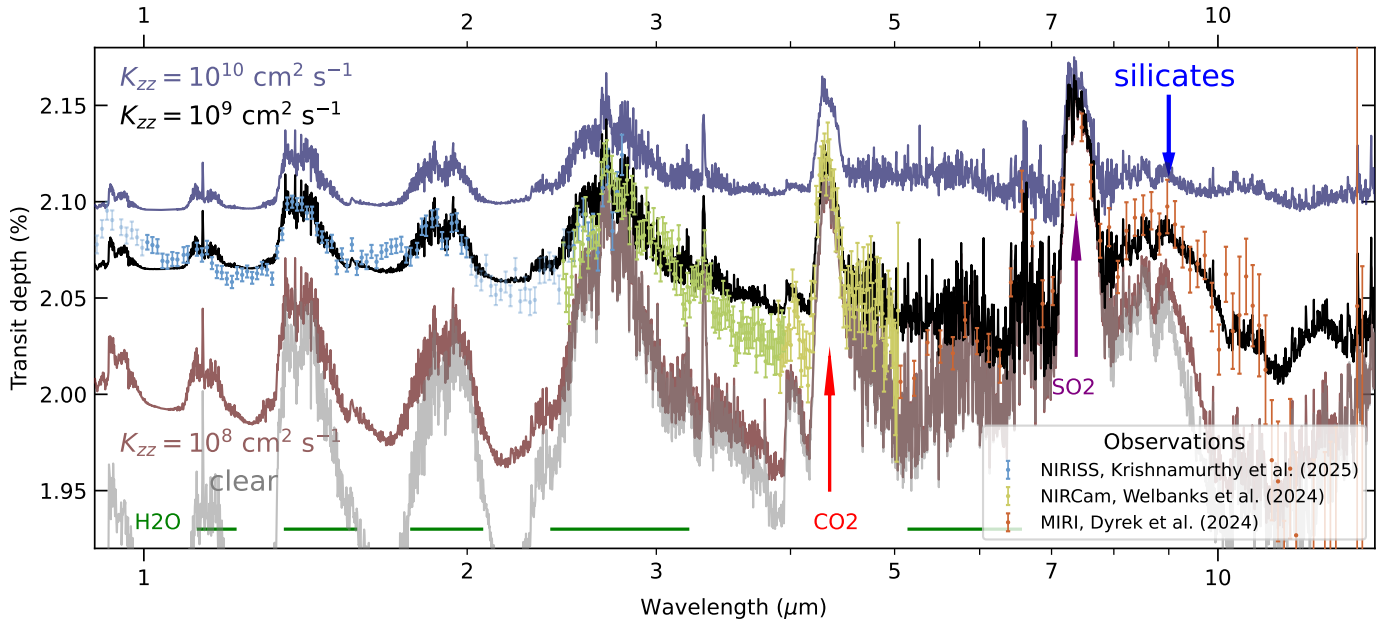


Fig. 2. JWST observations of WASP-107 b (colored vertical bars) along with the best fit model (black line; $K_{zz} = 10^9 \text{ cm}^2 \text{ s}^{-1}$), resulting in a $\chi^2_{\text{red}} = 3.4$. The NIRISS observations are shifted vertically by 130 ppm to match the NIRCams data at the wavelengths where they overlap. The runs with higher and lower K_{zz} are shown with blue and brown lines, respectively, to illustrate the spectroscopic effects of varying the turbulent diffusivity. The simulated spectrum of a cloudless atmosphere is plotted in gray.

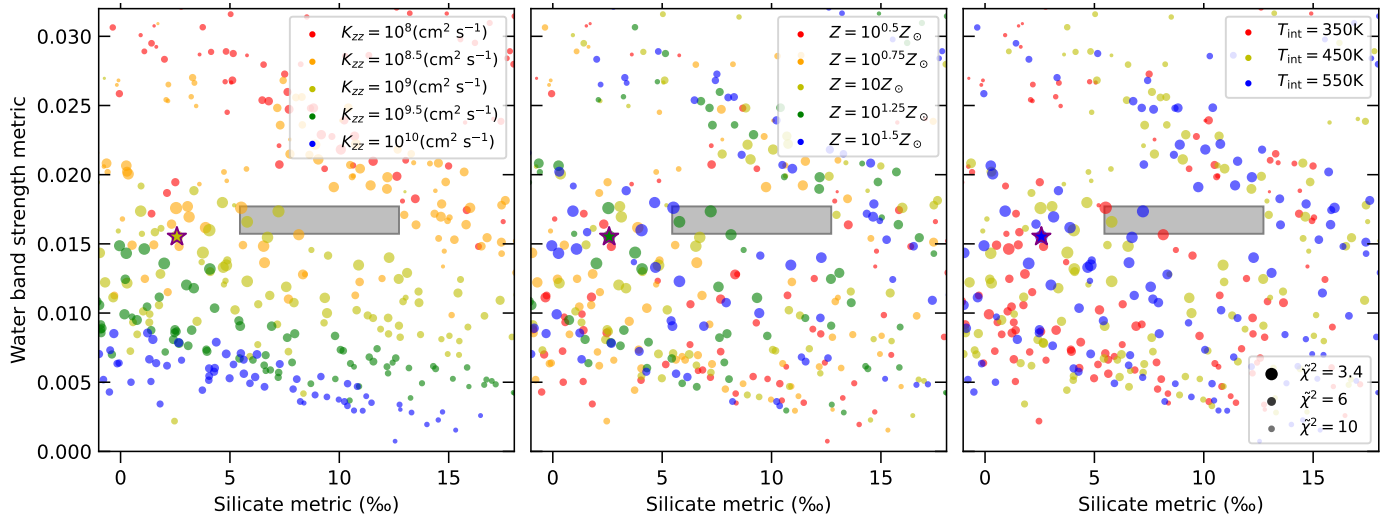


Fig. 3. Scatter plots demonstrating how the near-IR H_2O line strength and the $10 \mu\text{m}$ silicate metric depend on the diffusivity parameter (K_{zz} ; left), metallicity (Z ; middle) and internal energy flux (T_{int} ; right) model parameters. The size of the dots corresponds to the χ^2 of their fits to the JWST observations. The gray rectangle corresponds to the JWST observational data and their 1σ uncertainties. The best-fit model run (star), is in 2σ agreement with the observation.

$L_0 + L_1 P_1(\lambda) + L_2 P(\lambda)$. Then

$$f_{\text{silicate}} = (L_1^* - 2L_2^*)/L_0. \quad (2)$$

where "*" denote that L_1 is limited to the range $[-0.01L_0, 0]$ and $L_2 < 0$, respectively. The two terms encapsulate how the silicate feature manifests in the spectrum. Without silicates, the molecular opacity steeply decreases from $8\text{--}10 \mu\text{m}$ and f_{silicate} (through L_1) evaluates negatively. Silicate absorption reduces this decline: it flattens the opacity slope and increases f_{silicate} . With further increase of cloud thickness, a distinct absorption bump near $9 \mu\text{m}$ emerges, captured by L_2 . Defined in this way, the silicate metric indicates substantial evidence for silicates when f_{silicate} evaluates

≥ 0.01 . For WASP-107 b, the slope contribution (L_1) dominates and $f_{\text{silicate}} = 0.009$, indicating the likely presence of silicates.

Although a large scatter is present in Figure 3 due to the variation of parameters, a decreasing trend of f_{water} and slightly increasing trend of f_{silicate} is identified with increasing K_{zz} . The stronger turbulence dredges up more vapor to the upper atmosphere, where it condenses to form silicates and to suppress the molecular features. Increasing the metallicity directly leads to a higher H_2O abundance and stronger H_2O features. On the other hand, the metallicity and T_{int} parameter does not influence f_{water} and f_{silicate} in a systematic way. However, a hotter interior promotes quenching of CH_4 in the upper atmosphere, resulting in better fits to JWST observations (as indicated by the size of the

points): the average χ^2 of the top 10 best-fit runs decreases from 4.3 to 3.8 when increasing T_{int} from 350 K to 550 K. There are 3 models lying within 1σ from the observational constraints on the silicate metric and the water metric. These points, all with $\chi^2 < 3.7$, are statistically indistinguishable with the best-fit simulation. They all have parameters $K_{zz} \approx 10^9 \text{ cm}^2\text{s}^{-1}$ and $Z \approx 17$, confirming the robustness of our inferences.

Finally, the cloud profiles (and associated metrics) are mostly insensitive to nucleation parameters (not plotted). Higher nucleation rates are neutralized by coagulation while turbulence efficiently spreads cloud nuclei vertically (Huang et al. 2024).

3. Conclusions and Discussion

The cloud characteristics of WASP-107 b have been investigated using a model strategy that couples a two-stream radiative transfer model and a physically-motivated cloud formation model in a self-consistent manner. Our main findings are as follows:

1. The near-IR molecular band strength observed by JWST/NIRISS and NIRCams and the $10 \mu\text{m}$ silicate feature observed by JWST/MIRI can be reproduced simultaneously without assuming a parametrized cloud profile or temperature profile. Although the temperature in the upper atmosphere is relatively low compared to the condensation temperature of silicates, vertical updrafts lift cloud particles into the observable upper region.
2. The best-fit model employs a vertical turbulent diffusivity $K_{zz} = 10^9 \text{ cm}^2\text{s}^{-1}$, a value typical in exoplanet atmospheres (Kawashima & Min 2021; Baxter et al. 2021; Barat et al. 2025). When K_{zz} is lower, clouds become invisible due to gravitational settling, while higher K_{zz} dredges up too much cloud material, inconsistent with the relatively weak silicate feature.
3. Turbulence governs both the amplitude of the $10 \mu\text{m}$ silicate feature and the strength of the near-IR water lines. Self-consistently modeling the effect of turbulence on clouds (thickness, intensity) allows us to put tight constraints on K_{zz} .

The model used in this work eliminates excessive degrees of freedom compared to models adopting parametrized cloud opacity or TP profile. Despite consisting of just 1200 sets of parameters (Table 1), it is able to match the most prominent cloud features. With more and more JWST observations suggesting the presence of clouds on exoplanets (Grant et al. 2023; Inglis et al. 2024), the method could be applied in future (grid) retrievals.

Nevertheless, the 1D nature of the model is an assumption. Recently, differences in the morning vs evening limb spectrum have been pointed out on WASP-107 b (Murphy et al. 2024). The evening limb shows a stronger $2.7 \mu\text{m}$ H_2O feature and a higher transit depth, which suggests an atmosphere 100 K hotter than the morning limb. The relatively weak $10 \mu\text{m}$ silicate feature therefore may only originate from the evening limb, as silicate clouds would likely rain out in the cooler morning limb. The limb asymmetry likely also affects the photochemistry related to the SO_2 feature, as SO_2 can only form on the day side. A future effort would therefore be to integrate two limb models into our code, with different temperatures and compositions.

With its large radius for its mass, the super-puff WASP-107 b occupies a distinctive place in the exoplanet population. Similar to previous studies (S24 and W24), our modeling of the planet's atmospheric indicates a high internal temperature T_{int} , suggesting active internal heating, driven by, e.g. tidal or Ohmic dissipation (Batygin 2025; Tremblin et al. 2017). Notably, our inferred

atmospheric metallicity of 17x solar is consistent with the constraint in W24 but lower than the value reported by S24 – a finding that results from our self-consistent cloud model (see Appendix A.3). The slightly lower atmospheric metallicity leaves ample room for the bulk of the heavy elements to reside deep within the planet's interior.

Acknowledgements. This work was supported by the National Natural Science Foundation of China (NSFC) project no. 12473065 and 12233004. The authors thank Kazumasa Ohno and Sharon Xuesong Wang for insightful discussion, and the anonymous referee whose comments substantially improved the quality of the paper.

References

- Allard, N. F., Spiegelman, F., Leininger, T., & Molliere, P. 2019, A&A, 628, A120
- Anderson, D. R., Collier Cameron, A., Delrez, L., et al. 2017, A&A, 604, A110
- Azzam, A. A. A., Tennyson, J., Yurchenko, S. N., & Naumenko, O. V. 2016, MNRAS, 460, 4063
- Barat, S., Désert, J.-M., Mukherjee, S., et al. 2025, AJ, 170, 165
- Batygin, K. 2025, ApJ, 985, 87
- Baxter, C., Désert, J.-M., Tsai, S.-M., et al. 2021, A&A, 648, A127
- Borysow, A. 2002, A&A, 390, 779
- Borysow, A. & Frommhold, L. 1989, ApJ, 341, 549
- Borysow, A., Frommhold, L., & Moraldi, M. 1989, ApJ, 336, 495
- Borysow, A., Jorgensen, U. G., & Fu, Y. 2001, J. Quant. Spectr. Rad. Transf., 68, 235
- Borysow, J., Frommhold, L., & Birnbaum, G. 1988, ApJ, 326, 509
- Changeat, Q., Bardet, D., Chubb, K., et al. 2025, A&A, 699, A219
- Coles, P. A., Yurchenko, S. N., & Tennyson, J. 2019, MNRAS, 490, 4638
- Dominik, C., Min, M., & Tazaki, R. 2021, OpTool: Command-line driven tool for creating complex dust opacities, Astrophysics Source Code Library, record ascl:2104.010
- Dyrek, A., Min, M., Decin, L., et al. 2024, Nature, 625, 51
- Eddington, A. S. 1916, MNRAS, 77, 16
- Grant, D., Lewis, N. K., Wakeford, H. R., et al. 2023, ApJ, 956, L29
- Guillot, T. 2010, A&A, 520, A27
- Henning, T., Begemann, B., Mutschke, H., & Dorschner, J. 1995, A&AS, 112, 143
- Huang, H., Ormel, C. W., & Min, M. 2024, A&A, 691, A291
- Inglis, J., Batalha, N. E., Lewis, N. K., et al. 2024, ApJ, 973, L41
- Jäger, C., Dorschner, J., Mutschke, H., Posch, T., & Henning, T. 2003, A&A, 408, 193
- Kawashima, Y. & Min, M. 2021, A&A, 656, A90
- Koike, C., Kaito, C., Yamamoto, T., et al. 1995, Icarus, 114, 203
- Kreidberg, L., Line, M. R., Thorngren, D., Morley, C. V., & Stevenson, K. B. 2018, ApJ, 858, L6
- Krishnamurthy, V., Carteret, Y., Piaulet-Ghorayeb, C., et al. 2025, arXiv e-prints, arXiv:2505.20588
- Leconte, J. 2021, A&A, 645, A20
- Malik, M., Kitzmann, D., Mendonça, J. M., et al. 2019, AJ, 157, 170
- McKemmish, L. K., Masseron, T., Hoesijmakers, H. J., et al. 2019, MNRAS, 488, 2836
- Meador, W. E. & Weaver, W. R. 1980, Journal of the Atmospheric Sciences, 37, 630
- Mihalas, D. 1978, Stellar atmospheres
- Min, M., Hovenier, J. W., & de Koter, A. 2005, A&A, 432, 909
- Molliere, P., Wardenier, J. P., van Boekel, R., et al. 2019, A&A, 627, A67
- Murphy, M. M., Beatty, T. G., Schlawin, E., et al. 2024, Nature Astronomy, 8, 1562
- Palik, E. D. 1991, Handbook of optical constants of solids II
- Piaulet, C., Benneke, B., Rubenzahl, R. A., et al. 2021, AJ, 161, 70
- Pollack, J. B., Hollenbach, D., Beckwith, S., et al. 1994, ApJ, 421, 615
- Rackham, B. V., Apai, D., & Giampapa, M. S. 2018, ApJ, 853, 122
- Rothman, L. S., Gordon, I. E., Barber, R. J., et al. 2010, J. Quant. Spectr. Rad. Transf., 111, 2139
- Sing, D. K., Rustamkulov, Z., Thorngren, D. P., et al. 2024, Nature, 630, 831
- Spake, J. J., Sing, D. K., Evans, T. M., et al. 2018, Nature, 557, 68
- Stevenson, K. B. 2016, ApJ, 817, L16
- Stock, J. W., Kitzmann, D., & Patzer, A. B. C. 2022, MNRAS, 517, 4070
- Stock, J. W., Kitzmann, D., Patzer, A. B. C., & Sedlmayr, E. 2018, MNRAS, 479, 865
- Toon, O. B., Turco, R. P., Hamill, P., Kiang, C. S., & Whitten, R. C. 1979, Journal of the Atmospheric Sciences, 36, 718
- Tremblin, P., Chabrier, G., Mayne, N. J., et al. 2017, ApJ, 841, 30
- Tsai, S.-M., Lee, E. K. H., Powell, D., et al. 2023, Nature, 617, 483
- Welbanks, L., Bell, T. J., Beatty, T. G., et al. 2024, Nature, 630, 836
- Yee, S. W. & Vissapragada, S. 2025, arXiv e-prints, arXiv:2511.07746
- Yurchenko, S. N., Amundsen, D. S., Tennyson, J., & Waldmann, I. P. 2017, A&A, 605, A95
- Yurchenko, S. N., Mellor, T. M., Freedman, R. S., & Tennyson, J. 2020, MNRAS, 496, 5282
- Yurchenko, S. N., Tennyson, J., Syme, A.-M., et al. 2022, MNRAS, 510, 903

Table A.1. opacity data used in this work

Opacity source	Reference
Al ₂ O ₃ (s)	Koike et al. (1995)
Fe(s), MgO(s)	Palik (1991)
Fe ₂ O ₃ (s)	A.H.M.J. Triaud ^a
Mg ₂ SiO ₄ (s), MgSiO ₃ (s)	Jäger et al. (2003)
FeO(s)	Henning et al. (1995)
FeS(s)	Pollack et al. (1994)
H ₂ O, CO	Rothman et al. (2010)
CO ₂	Yurchenko et al. (2020)
CH ₄	Yurchenko et al. (2017)
H ₂ S	Azzam et al. (2016)
Na	Allard et al. (2019)
K	Mollière et al. (2019)
Mg, Fe, Al	K. Molaverdikhani ^b
SiO	Yurchenko et al. (2022)
TiO	McKemmish et al. (2019)
NH ₃	Coles et al. (2019)
H ₂ -H ₂	Borysow et al. (2001); Borysow (2002)
H ₂ -He	Borysow et al. (1988, 1989); Borysow & Frommhold (1989)

Notes. ^(a) <https://www.astro.uni-jena.de/Laboratory/OCDB/mgfeoxides.html> ^(b) <http://kurucz.harvard.edu/>

Appendix A: Methods

In this work we compute the self-consistent cloud structure and temperature profile by coupling the multi-species cloud code ExoLyn with a two-stream radiative transfer method. Here we briefly summarize the physical principles of our simulations. Details of our radiative transfer model are described in the companion paper.

Appendix A.1: Coupling between cloud formation and radiative transfer

ExoLyn (Huang et al. 2024) is a 1D cloud formation model that solves for the cloud composition, number density and size of the cloud particles. The cloud formation in ExoLyn is simulated as a chemical kinetics process instead of chemical equilibrium. For the cloud forming material, we assume C combines into CO and the leftover O forms H₂O, which applies for the hot deep atmosphere. Due to turbulence (eddy diffusion), molecules are transported to cooler, upper layers and condense into clouds. The reaction rates at which condensates form are evaluated using the local vapor concentration and the thermo-chemical property of the cloud forming reactions. Once formed, a cloud particle is subject to sedimentation, turbulent diffusion and coagulation, until it evaporates at the bottom of the atmosphere. The steady state cloud profile is solved using a computationally efficient relaxation method. During the cloud formation process, gas-phase chemical reactions are neglected, for simplicity. After a cloud structure has been obtained, the remaining gas species are forced to chemical equilibrium using FastChem (Stock et al. 2018, 2022).

Cloud formation depends sensitively on the temperature structure of the atmosphere. Therefore instead of leaving the temperature structure as free parameters, we seek to solve it self-consistently with cloud formation. The first step in radiative transfer calculation is to compute the cloud and gas phase opacity structure. For the cloud opacity, we take the same setting as Huang et al. (2024). Effective medium theory (Bruggeman rule) is applied to the composition of the cloud particles to get the average (effective) refractive index of the material mixture.

Then Optool (Dominik et al. 2021) is run to generate the cloud absorption and scattering opacity, assuming distribution of hollow spheres (DHS, Min et al. 2005) as the shape for the cloud particles. We use Exo-k (Leconte 2021) to mix the correlated-k tables of the individual gas species on the wavelength range from 0.3 μm to 50 μm , with a spectral resolution $R = 300$. The gas opacity sources included in the simulations are H₂O, CH₄, CO, CO₂, NH₃, H₂S, Na, K, Mg, Fe, Al, SiO, TiO and H₂-H₂, H₂-He collisional induced absorption, summarized in Table A.1.

Once the opacity is computed, we generalize the two-stream radiative transfer method in Guillot (2010) to get the temperature profile. The radiation field is decomposed into two components (Toon et al. 1979; Meador & Weaver 1980) – downward irradiation from the star in visible band and the upward irradiation from the planet interior in IR band. For both the IR and visual components, moment equations (Mihalas 1978) are solved, with the addition of Eddington approximation as closure condition (Eddington 1916). The location where the stellar energy is deposited is determined by the opacity distribution in the atmosphere, especially clouds, because they tend to absorb stellar visual photons efficiently. Applying energy balance – the radiation energy received by a layer equals to the blackbody radiation it emits – the temperature at a certain layer is computed. The assumptions and simplifications in the above method is benchmarked against the radiative transfer code PICASO in the companion paper. The temperature gradient computed from radiation transfer becomes super-adiabatic in the deep atmosphere (≥ 0.1 bar). In reality, convection transports the heat more efficiently in these region and homogenizes the temperature. We correct the super-adiabatic temperature gradient following the method presented in Malik et al. (2019), which guarantees that the temperature gradient is not larger than ∇_{ad} (assumed to be 2/7) and the net energy flux is conserved throughout the atmosphere.

In this work, ExoLyn and the radiative transfer code are coupled iteratively. Starting from a guess temperature profile, we compute the clouds structure and then the gas and cloud opacity. After this, the temperature corresponding to the opacity structure is computed to update the guess temperature. This process is run iteratively until convergence in temperature is reached. In the end, we generate the transmission spectra with petitRADTRANS (Mollière et al. 2019).

Appendix A.2: Adjustment to the equilibrium chemistry

Before computing the transmission spectrum, we made several adjustments to the gas profile under chemical equilibrium. It is found that the gas composition on WASP-107 b is affected by disequilibrium chemistry such as photochemistry and quenching (W24). For example, the JWST transmission spectrum of WASP-107 b shows the signal of SO₂, in contrast to H₂S predicted by chemical equilibrium. The SO₂ could be generated from oxidation of H₂S in photochemical reactions. However, as the main focus of this work is to understand the cloud features on WASP-107 b with a microphysical model, running a photochemistry model is beyond the scope of the model. Therefore, we artificially convert some fraction of H₂S to SO₂.

In addition, at the temperature akin to WASP-107 b, the presence of CH₄ and the absence of NH₃ is expected by equilibrium chemistry. However, the observed underabundance of CH₄ and overabundance of NH₃ are signposts of disequilibrium chemistry, specifically vertical quenching. Under strongly turbulent condition, CH₄-poor gas from the deep atmosphere is dredged up into the visible, upper atmosphere, and vice versa, reducing the concentration of CH₄. As simulating disequilibrium chemistry

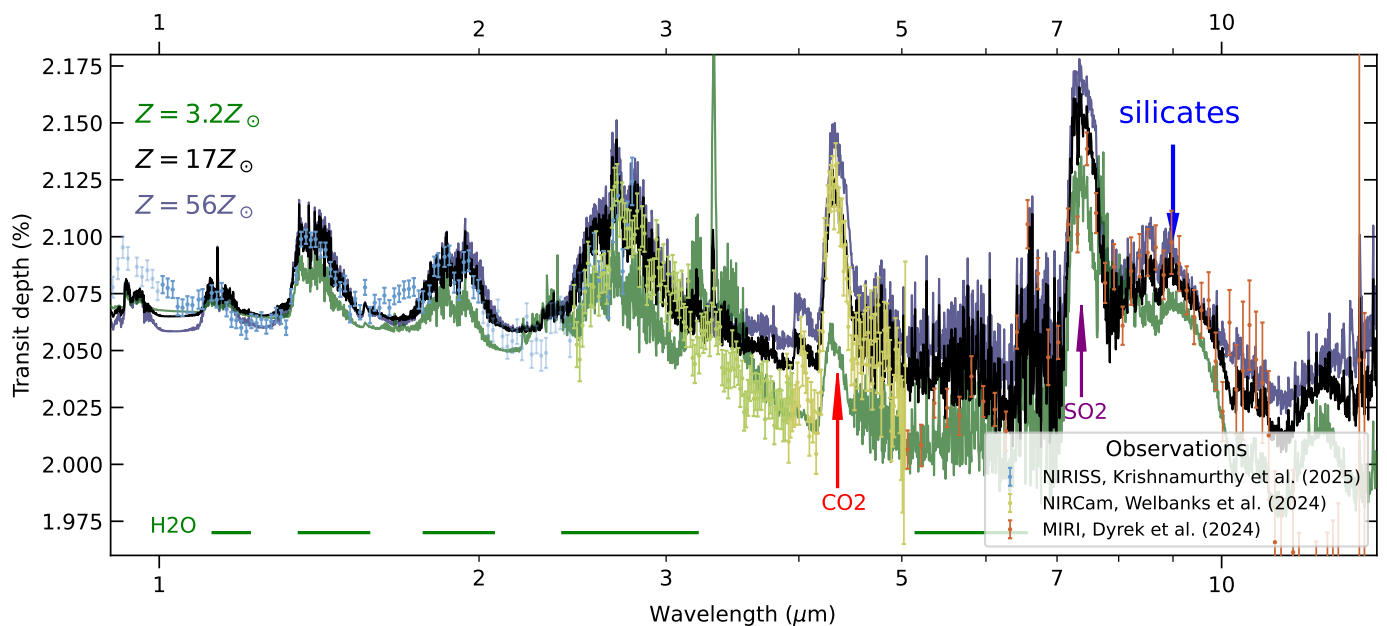


Fig. A.1. Same as Figure 2, but with metallicity $Z = 56 Z_{\odot}$ and $Z = 3.2 Z_{\odot}$. For each metallicity, the control parameters (Appendix A.2) are kept the same as the best-fit model.

is beyond the scope of this work, we mimic the above effects by postprocessing the gas profile before generating the transmission spectrum:

- We convert a fraction of $f_{\text{H}_2\text{S}}$ H_2S to SO_2 .
- We replace all molecular abundances above a quenching pressure P_{quench} with those values at that location.

For each parameter set in Table 1, the best-fit $f_{\text{H}_2\text{S}}$, P_{quench} and the reference pressure P_{ref} at which the planet radius is measured are optimized by the conjugate gradient method. The best fit parameters in Figure 2 have $f_{\text{H}_2\text{S}} = 9 \times 10^{-3}$, $P_{\text{quench}} = 0.06$ bar.

Our model manages to fit the $7.2 \mu\text{m}$ SO_2 feature, but undershoot the $4 \mu\text{m}$ SO_2 feature. The reason could be that the cloud extinction in our model is slightly stronger than it is suggested by the $4 \mu\text{m}$ SO_2 feature. Therefore, tuning a smaller K_{zz} could lead to a slightly clearer atmosphere and decrease the transit depth redward to the SO_2 feature, providing a better fit. Note that the SO_2 concentration in this work is calculated by simply converting 0.6% of H_2S to SO_2 , translating to a nearly constant volume mixing ratio $\approx 10^{-6}$ at all locations in atmosphere. W24 applied a 1D radiative-convective-photochemical equilibrium (RCPE) model, which found that SO_2 only form around a level of 10^{-5} bar, with the peak volume mixing ratio 10^{-4} . Explaining the presence of SO_2 with a cloudy RCPE model is left to a future work.

Appendix A.3: Higher metallicity simulations

The best-fit atmospheric metallicity in our work, $Z = 17 Z_{\odot}$, is consistent with the constraint from W24 ($10\text{--}18 Z_{\odot}$) and with the K abundance from K25 ($8_{-6}^{+26} Z_{\odot}$). However, it is lower than the values reported by S24 ($43 \pm 8 Z_{\odot}$). Motivated by their constraint, we simulate a metal-rich ($Z = 56 Z_{\odot}$) and a low metallicity ($Z = 3.2 Z_{\odot}$) model to understand how metallicity affects the spectrum. The control parameters described in Appendix A.2 are kept the same as those of the best-fit model for each metallicity. The results are shown in Figure A.1.

With a $\chi^2 = 6.5$, the metal-rich atmosphere with $Z = 56 Z_{\odot}$ offers a worse fit. Although a higher metallicity of $56 Z_{\odot}$ elevates the mean molecular weight to 3.07, its effect on the scale height is not strong enough to suppress the gas and cloud features. The amplitude of the H_2O features at $1.4 \mu\text{m}$ and the CO_2 feature at $4.3 \mu\text{m}$ are overestimated compared to the observations. Increasing the metallicity results in a higher H_2O abundance and enhances the corresponding features in the near-IR band. The CO_2 abundance is especially sensitive to metallicity, with its signal at $4.3 \mu\text{m}$ enhanced from 400 ppm for $3.2 Z_{\odot}$ to 900 ppm for $56 Z_{\odot}$. The silicate feature at $10 \mu\text{m}$ is not sensitive to metallicity. Although more vapor condenses in metal-rich atmosphere, the silicate-bearing cloud particles gravitationally settle to optically opaque layers once the particles grow larger.

The unusual large radius of WASP-107 b requires a large envelope mass fraction and small core mass of $5M_{\oplus}$ (Piaulet et al. 2021). However, this poses a question to the formation theory how such low mass core accreted an envelope of $25M_{\oplus}$. The strong internal heating (T_{int}) inferred in our model, W24 and S24, suggests a hotter envelope and helps to explain the inflated radius of the planet without involving a small core mass fraction. This intense interior radiation potentially stems from the tidal heating related to the planet’s moderate eccentricity $e \sim 0.05$ (Piaulet et al. 2021; Murphy et al. 2024; Yee & Vissapragada 2025) or from the Ohmic dissipation in the planet interior (Batygin 2025).